Actuator nonlinear fault-tolerant control of a fast-spinning quadrotor with loss of two opposing rotors

T.M.L. De Ponti*, E.J.J. Smeur and B.W.D. Remes
Delft University of Technology, 2629 HS Delft, The Netherlands

http://www.imavs.org/

ABSTRACT

The problem of maintaining control of a quadcopter following the failure of motors is well established within the Fault Tolerant Control (FTC) community. While Incremental Nonlinear Dynamic Inversion (INDI) has been successfully applied to achieve relaxed hover in multirotors under opposing motor failures, its framework typically assumes infinitely fast actuators and neglects state-dependent effects. However, for a quadcopter in a failure scenario where two opposing motors are lost, the vehicle must spin rapidly to stabilize. At high spin rates, the gyroscopic stabilization effect becomes significant, and the assumption of negligible state effects becomes unreasonable. To address this limitation, this paper investigates the use of Actuator Nonlinear Dynamic Inversion (ANDI), a refined control strategy that explicitly incorporates actuator dynamics and state-induced effects into the control allocation. Through theoretical analysis, simulation, and real-world flight tests at the TU Delft indoor test facility, the proposed ANDI controller is directly compared to a baseline INDI controller. The results demonstrate that by compensating for state-induced gyroscopic effects, the ANDI framework is capable of guiding and stabilizing the quadcopter at significantly higher spin rates than INDI. Furthermore, the ANDI controller exhibits better control allocation, evidenced by a lower control effort variance during stationary flight compared to INDI. To the best of the authors' knowledge, this work presents the first successful real-world flight demonstration of an ANDI controller applied to a quadcopter under the failure of two opposing motors.

1 INTRODUCTION

The problem of maintaining control of a quadcopter following the failure of one or more motors is a well-established challenge within the Fault Tolerant Control (FTC) community. [1] first introduced the periodic solution to the so-called reduced-attitude (or relaxed-hover) problem for cases involving one, two, or three failed motors. Subsequently, [2] demonstrated that this solution could be realized in practice using an Linear Quadratic Regulator (LQR). An alternative and highly effective control strategy for the relaxed-hover problem is Incremental Nonlinear Dynamic Inversion (INDI), as proposed by [3] and [4].

INDI has been successfully applied across a broad range of platforms, including multirotors [5], fixed-wing aircraft [6], Vertical Take-Off and Landing (VTOL) vehicles [7], and helicopters [8]. Its primary advantages over traditional controllers include rapid disturbance rejection [5, 6, 9], a reduced need for gain scheduling, and a minimized reliance on accurate model information due to its sensor-based formulation [10]. In [3], these disturbance-rejection capabilities were exploited to achieve relaxed hover in the presence of varying airspeed with a single failed motor. [4] further extended this high-speed INDI FTC framework to accommodate the failure of two motors. More recently, in [11], INDI was applied to control a large quad-plane experiencing a failure of two opposing motors.

In the standard INDI framework, actuator dynamics are not explicitly modeled, and state-dependent effects are typically neglected. This simplification is often justified by assuming that state effects evolve slowly compared to the fast response of the actuators, as discussed in [12]. However, this assumption breaks down when state-induced effects are highly dynamic or when the system utilizes actuators with varying response times.

To address this limitation, the work of [13] reformulated the INDI control law, modifying the control effectiveness matrix used in the allocation process to explicitly account for actuator dynamics [14]. Building on this, the methods presented in [13], [15], and [16] derived the control law by taking an additional time derivative of the system output, seamlessly incorporating actuator dynamics directly into the effectiveness matrix. This refined control strategy, referred to as Actuator Nonlinear Dynamic Inversion (ANDI) in [16], enhances the compensation of actuator lag and improves overall system stability. The framework established in [16] was later extended to more generalized actuator dynamics in [17]. Furthermore, [18] and [19] exploited ANDI to control systems featuring heterogeneous actuator dynamics, demonstrating clear improvements over standard INDI. In contrast, [20] focused on analyzing the benefits of using ANDI to compensate for state effects arising from aerodynamic interactions of a winged platform, concluding that the performance improve-

*Email address: tmldeponti@tudelft.nl

http://www.imavs.org/

ment over INDI was marginal because the aerodynamic state effects were small and evolved slowly.

Despite these advancements, little research has addressed the application of ANDI in scenarios where state-dependent effects are highly significant and evolve as rapidly as the actuator responses themselves. The reduced-attitude control of a quadcopter presents an ideal test case for this problem, as the gyroscopic stabilization effects inherent to a rapidly spinning body cannot be deemed negligible, especially for platforms with specific inertia distributions operating at high spin rates. Crucially, the faster the required spin rate, the closer the frequency of the state-induced effects approaches the bandwidth of the actuator dynamics. Such scenarios are particularly relevant for heavy-lift quadcopters. These platforms typically feature relatively compact, aerodynamic bodies paired with large motors and propellers. In the event of two opposing motors failing, the substantial aerodynamic drag of the propellers requires the drone to spin rapidly to maintain lift. Concurrently, larger motors inherently possess slower dynamic responses, rendering the standard INDI assumption of infinitely fast actuators and negligible state effects unreasonable.

To address this gap in the literature, the main contributions of this paper are twofold: (1) to the best of the authors' knowledge, this work presents the first successful real-world flight demonstration of an ANDI controller applied to a quadcopter experiencing a complete failure of two opposing motors; (2) a comprehensive comparative analysis between the proposed ANDI framework and a baseline INDI controller, demonstrating the operational limits and control allocation benefits of explicitly accounting for gyroscopic state effects.

2 SYSTEM MODEL

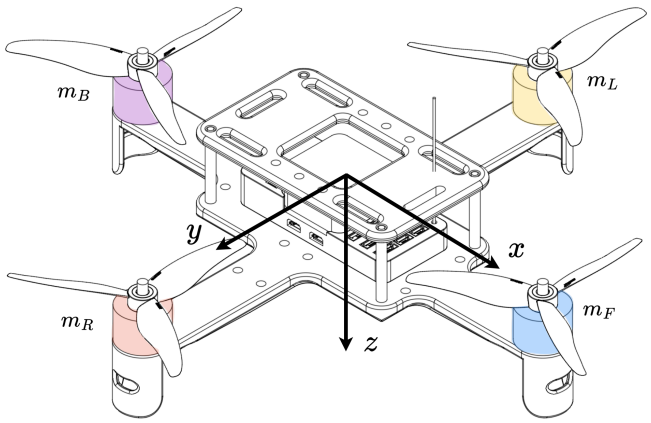


Figure 1: The quadcopter used in the experiments with body axis definition.

The drone utilized in the experiments, along with the body axis definition, is shown in Figure 1. The drone is equipped with four identical motors, denoted as m_F, m_R, m_B, and m_L for the front, right, back, and left motors, respectively. It is assumed that the motors exhibit first-order dynamics with corner freqeuncy ε. Furthermore, the thrust generated by each motor is modeled as being proportional to the square of its rotational speed, such that:

$$T_i = k_T \omega_i^2, \tag{1}$$

where T_i is the thrust generated by the i-th motor, k_T is the thrust coefficient, and ω_i is the rotational speed. Consequently, the control force $\boldsymbol{F}_c$ exerted in the body frame is given by:

$$\begin{bmatrix} F_{c_x} \\ F_{c_y} \\ F_{c_z} \end{bmatrix} = \begin{bmatrix} 0 & 0 & 0 & 0 \\ 0 & 0 & 0 & 0 \\ -k_T & -k_T & -k_T & -k_T \end{bmatrix} \begin{bmatrix} \omega_F^2 \\ \omega_R^2 \\ \omega_B^2 \\ \omega_L^2 \end{bmatrix}. \tag{2}$$

All motors are located at the same distance l from the center of gravity. Thus, the resulting control moment $\boldsymbol{M}_c$ exerted in the body frame is modeled as:

$$\begin{bmatrix} M_{c_x} \\ M_{c_y} \\ M_{c_z} \end{bmatrix} = \begin{bmatrix} 0 & -lk_T & 0 & lk_T \\ lk_T & 0 & -lk_T & 0 \\ -\tau & \tau & -\tau & \tau \end{bmatrix} \begin{bmatrix} \omega_F^2 \\ \omega_R^2 \\ \omega_B^2 \\ \omega_L^2 \end{bmatrix}. \tag{3}$$

Here, the reaction torque produced by the motors is also modeled as being proportional to the square of the rotational speed, with a proportionality coefficient τ. The inertia tensor of the platform is assumed diagonal with principal moments of inertia I_{xx}, I_{yy}, and I_{zz}. Finally Table 1 reports the parameters of the model of the platform.

Parameter	Vaule	Unit
m	9.38e-1	kg
I_{xx}	2.70e-3	$\mathrm{kg\,m^2}$
I_{yy}	3.60e-3	$\mathrm{kg\,m^2}$
I_{zz}	4.50e-3	$\mathrm{kg\,m^2}$
k_T	7.564e-7	$\mathrm{N\,s^2\,rad^{-2}}$
τ	7.657e-9	$\mathrm{N\,m\,s^2\,rad^{-2}}$
ε	29.0	$\mathrm{rad\,s^{-1}}$
l	1.30e-1	m

Table 1: Parameters of the quadcopter.

3 CONTROL LAWS

Both the ANDI and INDI control laws, as for example shown in [11] and [18],can be derived for a general nonlinear system by assuming first-order actuator dynamics and infinitely fast actuators, respectively. Consider a system with output $\boldsymbol{y} \in \mathbb{R}^m$, state vector $\boldsymbol{x} \in \mathbb{R}^k$, and actuator state vector $\boldsymbol{u} \in \mathbb{R}^n$, governed by:

$$\dot{\boldsymbol{x}} = \boldsymbol{f}(\boldsymbol{x}, \boldsymbol{u}), \quad \boldsymbol{y} = \boldsymbol{h}(\boldsymbol{x}). \tag{4}$$

http://www.imavs.org/

The system has a relative degree r with respect to $\boldsymbol{u}$ (i.e., the output $\boldsymbol{y}$ must be differentiated r times before the input $\boldsymbol{u}$ appears explicitly [16]), such that:

$$\boldsymbol{y}^{(r)} = \boldsymbol{F}(\boldsymbol{x}, \boldsymbol{u}). \tag{5}$$

Taking an additional time derivative yields:

$$\boldsymbol{y}^{(r+1)} = \frac{\partial \boldsymbol{F}}{\partial \boldsymbol{x}}\,\dot{\boldsymbol{x}} + \frac{\partial \boldsymbol{F}}{\partial \boldsymbol{u}}\,\dot{\boldsymbol{u}} = \boldsymbol{F}_x\,\dot{\boldsymbol{x}} + \boldsymbol{F}_u\,\dot{\boldsymbol{u}}. \tag{6}$$

For notational simplicity, we assume $r = 1$. Next, consider stable actuator dynamics of degree d, described by the transfer function:

$$A = \frac{U}{U_c} = \frac{\prod_{i=1}^{d}(-\varepsilon_i)}{\prod_{i=1}^{d}(s - \varepsilon_i)}, \tag{7}$$

where ε_i denotes the i-th pole with $\Re\{\varepsilon_i\} < 0$, and capital letters indicate variables expressed in the Laplace domain. Here, U_c denotes the commanded actuator input and U the realized actuator state after actuator dynamics. For the multiple input multiple output (MIMO) case, $\boldsymbol{A} \in \mathbb{R}\,(s)^{n\times n}$ is a diagonal matrix of transfer functions. The incremental commanded control input can then be defined in terms of the actuator dynamics as:

$$\boldsymbol{\Delta U} = \boldsymbol{U_c} - \boldsymbol{U} = \big(\boldsymbol{I} - \boldsymbol{A}\big)\,\boldsymbol{U_c}. \tag{8}$$

From Eq. (8), it follows that:

$$\mathcal{L}\{\dot{\boldsymbol{u}}\} = s\boldsymbol{U} = s\boldsymbol{A}\boldsymbol{U_c} = s\boldsymbol{A}\,[\boldsymbol{I} - \boldsymbol{A}]^{-1}\,\boldsymbol{\Delta U} = \boldsymbol{W}\,\boldsymbol{\Delta U}. \tag{9}$$

Let the pseudo-control vector $\boldsymbol{\nu} \in \mathbb{R}^m$ (denoted as $\boldsymbol{N}$ in the Laplace domain) represent the desired system output $\boldsymbol{y}_d$. Additionally, we define the transfer function matrix $\boldsymbol{V} \in \mathbb{R}\,(s)^{m\times m}$, which maps the tracking error $\boldsymbol{e} = \boldsymbol{\nu} - \boldsymbol{y}$ to $\dot{\boldsymbol{y}}$:

$$\mathcal{L}\{\dot{\boldsymbol{y}}\} = s\boldsymbol{Y} = \boldsymbol{V}\big(\boldsymbol{N} - \boldsymbol{Y}\big). \tag{10}$$

To maximize performance without overdriving the actuators, a natural design choice is to match the desired closed-loop output dynamics along each axis directly to the bandwidth of the slowest influencing actuator. Substituting $Y = AN$ into Eq. (10) for each individual control axis and rearranging gives:

$$sAN = V\big(1 - A\big)N \Longleftrightarrow V = sA(1 - A)^{-1} = W. \tag{11}$$

Assuming $\boldsymbol{F}_x$ and $\boldsymbol{F}_u$ are approximately constant over one control step, we can substitute Eqs. (9) to (11) into Eq. (6) and rearrange to obtain the general closed-loop expression:

$$\begin{aligned} \boldsymbol{V}\big(\boldsymbol{N} - \boldsymbol{Y}\big) &= \boldsymbol{F}_u\boldsymbol{W}\boldsymbol{\Delta U} + \boldsymbol{F}_x s\boldsymbol{X}, \\ \boldsymbol{\Delta U} &= \big(\boldsymbol{F}_u\boldsymbol{W}\big)^{+}\Big(\boldsymbol{V}\big(\boldsymbol{N} - \boldsymbol{Y}\big) - \boldsymbol{F}_x s\boldsymbol{X}\Big). \end{aligned} \tag{12}$$

3.1 INDI

The INDI approach assumes infinitely fast actuators. Equation (7) implies that as the actuator dynamics become infinitely fast (i.e., $\Re\{\varepsilon_i\} \to -\infty$), $A \to 1$, which consequently means $W \to \infty$ and $V \to \infty$. Under this assumption, Eq. (12) reduces to the INDI control law:

$$\begin{aligned} \boldsymbol{\Delta U} &= \big(\boldsymbol{F}_u\big)^{+}\big(\boldsymbol{N} - \boldsymbol{Y}\big), \\ \boldsymbol{\Delta u} &= \big(\boldsymbol{F}_u\big)^{+}\big(\boldsymbol{\nu} - \boldsymbol{y}\big). \end{aligned} \tag{13}$$

In this control law, $\boldsymbol{F}_u$ is commonly referred to as the control effectiveness matrix.

3.2 ANDI

In contrast, ANDI explicitly accounts for first-order actuator dynamics:

$$A = \frac{\varepsilon}{s + \varepsilon}. \tag{14}$$

It follows that $\boldsymbol{W}$ is a diagonal matrix containing the corner frequency of each actuator:

$$\boldsymbol{W} = \begin{bmatrix} \varepsilon_{u_1} & & \\ & \ddots & \\ & & \varepsilon_{u_n} \end{bmatrix}, \tag{15}$$

while $\boldsymbol{V}$ is a diagonal matrix containing the corner frequency of the slowest actuator associated with each controlled axis:

$$\boldsymbol{V} = \begin{bmatrix} \varepsilon_{\nu_1} & & \\ & \ddots & \\ & & \varepsilon_{\nu_m} \end{bmatrix}. \tag{16}$$

For a fully actuated system with identical actuators, it is clear that $\boldsymbol{W} = \boldsymbol{V}$, which simplifies the control law to:

$$\begin{aligned} \boldsymbol{\Delta U} &= \big(\boldsymbol{F}_u\big)^{+}\,(\boldsymbol{N} - \boldsymbol{Y}) - \big(\boldsymbol{F}_u\boldsymbol{W}\big)^{+}\,(\boldsymbol{F}_x s\boldsymbol{X})\,, \\ \boldsymbol{\Delta u} &= \big(\boldsymbol{F}_u\big)^{+}\,(\boldsymbol{\nu} - \boldsymbol{y}) - \big(\boldsymbol{F}_u\boldsymbol{W}\big)^{+}\,(\boldsymbol{F}_x\dot{\boldsymbol{x}})\,. \end{aligned} \tag{17}$$

Equation (17) highlights a fundamental operational difference between ANDI and INDI: ANDI explicitly compensates for the state-driven term $\boldsymbol{F}_x s\boldsymbol{X}$ in its control allocation.

4 STATE EFFECT

To illustrate the effect of neglecting the state-driven term, consider the problem of controlling the roll angular acceleration of a spinning gyroscope with the same physical parameters of the test platform as reported in Section 2. A constant yaw moment M_z is applied to the gyroscope, resulting in a continuously increasing yaw rate. The controller aims to track a desired roll angular acceleration $\dot{p}_d$ by manipulating the moment exerted about the body x-axis, M_x. This moment is generated by a first-order actuator with corner frequency ε and is proportional to its state u, such that

$$M_x = k_x u. \tag{18}$$

Aerodynamic effects and other disturbances are neglected, so that $M_y = 0$. From Euler's equations for the rotational motion of a rigid body, expressed in the body frame, it follows that

$$\begin{bmatrix}\dot{p}\\ \dot{q}\\ \dot{r}\end{bmatrix} = \begin{bmatrix}\frac{k_x u}{I_{xx}} - \frac{I_{zz}-I_{yy}}{I_{xx}}qr\\ -\frac{I_{xx}-I_{zz}}{I_{yy}}pr\\ M_z - \frac{I_{yy}-I_{xx}}{I_{zz}}pq\end{bmatrix} = \begin{bmatrix}\frac{k_x u}{I_{xx}} + C_x qr\\ C_y pr\\ M_z + C_z pq\end{bmatrix}. \quad (19)$$

Taking one extra derivative in time leads to:

$$\begin{bmatrix}\ddot{p}\\ \ddot{q}\\ \ddot{r}\end{bmatrix} = \underbrace{\begin{bmatrix}\frac{k_x}{I_{xx}}\\ 0\\ 0\end{bmatrix}}_{F_u}\dot{u} + \underbrace{\begin{bmatrix}0 & C_x r & C_x q\\ C_y r & 0 & C_y p\\ C_z q & C_z p & 0\end{bmatrix}}_{F_x}\begin{bmatrix}\dot{p}\\ \dot{q}\\ \dot{r}\end{bmatrix}. \quad (20)$$

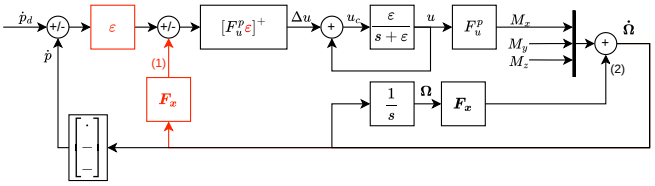


Figure 2: Structure for the gyro controller. Red signals and blocks are only present in ANDI.

The control structure of an ANDI controller (red signals included) is shown in Figure 2. It uses the control law of Eq. (17), designed to track a desired roll angular acceleration using the roll effectiveness F_u^p, i.e., the entry of $\boldsymbol{F_u}$ corresponding to the roll axis. In particular, by rearranging the diagram, it can be shown that the state compensation signal (1) cancels the state effect on the controlled signal (2). In other words, because the state compensation is embedded directly in the control law, ANDI tracks $\dot{p}_d$ with the same dynamics regardless of the gyroscope spin rate. More precisely, as discussed in Section 3, these dynamics are equal to the actuator dynamics.

Figure 2 also shows the control structure of an INDI controller (red signals excluded), which uses the control law of Eq. (13), designed to perform the same task. It is clear that, unless $\boldsymbol{F_x}$ or $\boldsymbol{\Omega}$ is zero, the closed-loop dynamics differ from the actuator dynamics. The controller allocates the actuator input while completely neglecting the effect of the state on the controlled signal. As the yaw rate r increases, the gyroscopic coupling becomes progressively stronger, and neglecting this effect is therefore expected to degrade performance.

This conclusion is confirmed by the simulation shown in Figure 3, in which the gyroscope spins increasingly faster about the yaw axis. ANDI is able to track the desired sinusoidal $\dot{p}$ accurately, with dynamics matching those of the actuator $\dot{p}_{dyn}$, whereas INDI exhibits increasing attenuation and lead as r grows. The INDI behavior can also be confirmed analytically by linearizing the nonlinear plant around

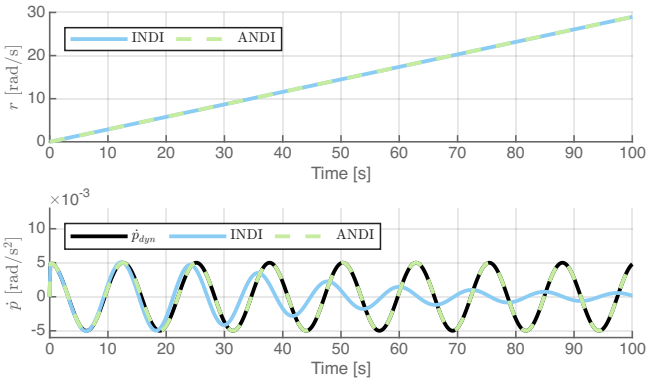


Figure 3: Simulation of a spinning gyroscope.

a trim condition $z = [p_0, q_0, r_0]^T$, where r_0 is constant and non-zero and the remaining angular rates are zero. This allows the linearized dynamics to be expressed in state-space form as:

$$\begin{bmatrix}\dot{p}\\ \dot{q}\\ \dot{r}\end{bmatrix} = \underbrace{\begin{bmatrix}0 & C_x r_0 & 0\\ C_y r_0 & 0 & 0\\ 0 & 0 & 0\end{bmatrix}}_{A}\begin{bmatrix}p\\ q\\ r\end{bmatrix} + \underbrace{\begin{bmatrix}\frac{k_x}{I_{xx}}\\ 0\\ 0\end{bmatrix}}_{B}u. \quad (21)$$

The resulting transfer function for the tracking dynamics of the INDI controller is given by:

$$\frac{\dot{p}}{\dot{p}_d}(s)_I = \frac{\varepsilon\, s}{s^2 + \varepsilon\, s - C_x\, C_y\, {r_0}^2}. \quad (22)$$

Equation (22) shows how the INDI controller behaves as a second-order system with a zero at the origin and a pair of complex conjugate poles. As r_0 increases, the poles move further to the right in the complex plane, resulting in increased attenuation and phase lead at frequencies below the actuator bandwidth. Such system reduces to the actuator dynamics only when $r_0 = 0$, which is the condition under which the state effect is negligible and the INDI assumption holds.

A Bode plot for the transfer function in Eq. (22) is shown in Figure 4. It confirms that as r_0 becomes larger, the controller increasingly attenuates the signal and introduces phase lead at frequencies below the actuator's bandwidth.

Consequently, for a rapidly spinning body, such as a gyroscope or a quadcopter experiencing a failure of two opposing motors, the INDI approach is expected to suffer from progressively degraded performance as the spin rate increases. In contrast, ANDI will properly compensate for these state-dependent effects and maintain the expected actuator dynamics.

5 REDUCED ATTITUDE

When a quadcopter loses two opposing motors, it becomes underactuated and can no longer independently control all its attitude degrees of freedom. Typically, yaw control

http://www.imavs.org/

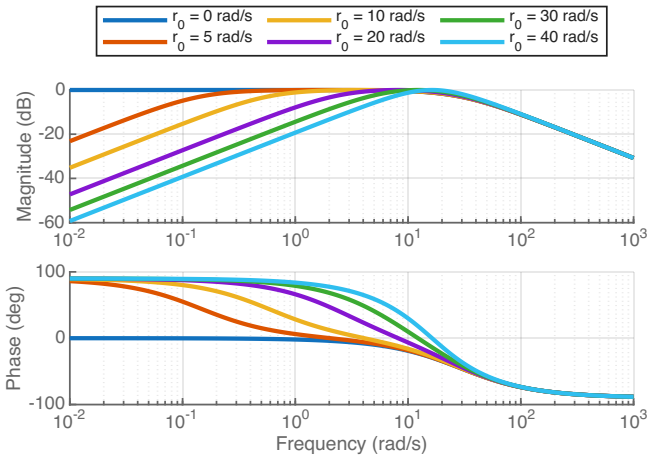


Figure 4: Bode plot of the INDI dynamics at different yaw rates.

is sacrificed, causing the vehicle to spin continuously about its vertical axis. This necessitates a control framework that can still achieve stabilization independently of the yaw angle, a method commonly known as the reduced attitude control problem.

The key idea is to regulate the principal axis of rotation, expressed in the body frame as $\boldsymbol{\mu}^B \in \mathbb{R}^3$, such that it tracks a desired inertial direction $\boldsymbol{n}^I \in \mathbb{R}^3$. To apply ANDI or INDI to this problem, we differentiate the relevant kinematics until the actuator states appear explicitly, and then differentiate once again with respect to time, as shown in Eq. (6).

Let $\boldsymbol{n}^I$ and $\boldsymbol{n}^B$ denote the same geometric vector expressed in the inertial and rotating body frames respectively such that:

$$\boldsymbol{n}^B = \boldsymbol{L}_{BI}\, \boldsymbol{n}^I, \tag{23}$$

where $\boldsymbol{L}_{BI}$ is the rotation matrix from the inertial frame to the body frame. The time derivative of $\boldsymbol{n}^B$ observed in the inertial frame is given by: The time derivatives of a generic vector $\boldsymbol{Q}$ observed in these frames are related by the transport theorem:

$$\left(\left.\frac{d\boldsymbol{Q}}{dt}\right|_I\right)^B = \left(\left.\frac{d\boldsymbol{Q}}{dt}\right|_B\right)^B + \boldsymbol{\omega}^B \times \boldsymbol{Q}^B, \tag{24}$$

where the superscript indicates the frame in which the quantity is expressed, and the subscript indicates the frame with respect to which the derivative is taken. Higher-order derivatives are obtained through repeated application of Eq. (24). Compactly, the m-th derivative is:

$$\left(\left.\frac{d^m\boldsymbol{Q}}{dt^m}\right|_I\right)^B = \left[\frac{d(*)}{dt} + \boldsymbol{\omega}^B \times (*)\right]^{(m)} \boldsymbol{Q}^B, \tag{25}$$

where $[\,\cdot\,]^{(m)}$ denotes m successive applications of the operator in brackets.

Using this result, one can derive expressions for the time derivatives of $\boldsymbol{n}^B$ as observed in the body frame. For the first derivative:

$$(\dot{\boldsymbol{n}}|_B)^B = -\boldsymbol{\omega}^B \times \boldsymbol{n}^B + (\dot{\boldsymbol{n}}|_I)^B, \tag{26}$$

and for the second derivative:

$$\begin{aligned}(\ddot{\boldsymbol{n}}|_B)^B = &-(\dot{\boldsymbol{\omega}}|_B)^B \times \boldsymbol{n}^B + \boldsymbol{\omega}^B \times \left(\boldsymbol{\omega}^B \times \boldsymbol{n}^B\right) \\ &- 2\,\boldsymbol{\omega}^B \times (\dot{\boldsymbol{n}}|_I)^B + (\ddot{\boldsymbol{n}}|_I)^B.\end{aligned} \tag{27}$$

The term $-(\dot{\boldsymbol{\omega}}|_B)^B \times \boldsymbol{n}^B$ can be written more conveniently in matrix form by introducing the skew-symmetric cross-product matrix associated with $\boldsymbol{n}^B$. Defining

$$\boldsymbol{H}_B = [\boldsymbol{n}^B]_\times = \begin{bmatrix} 0 & -n_z^B & n_y^B \\ n_z^B & 0 & -n_x^B \\ -n_y^B & n_x^B & 0 \end{bmatrix}, \tag{28}$$

and using the property $\boldsymbol{a} \times \boldsymbol{b} = [\boldsymbol{a}]_\times \boldsymbol{b}$, we obtain:

$$-(\dot{\boldsymbol{\omega}}|_B)^B \times \boldsymbol{n}^B = \boldsymbol{n}^B \times (\dot{\boldsymbol{\omega}}|_B)^B = \boldsymbol{H}_B\, \dot{\boldsymbol{\omega}}^B. \tag{29}$$

From Euler's equations for the rotational motion of a rigid body about a fixed point, expressed in the body frame, we have:

$$\boldsymbol{I}\, \dot{\boldsymbol{\omega}}^B = \boldsymbol{M}(\boldsymbol{u}, \boldsymbol{x}) - \boldsymbol{\omega}^B \times \left(\boldsymbol{I}\boldsymbol{\omega}^B\right), \tag{30}$$

which yields:

$$\dot{\boldsymbol{\omega}}^B = \boldsymbol{I}^{-1}\boldsymbol{M}(\boldsymbol{u}, \boldsymbol{x}) - \boldsymbol{I}^{-1}\left(\boldsymbol{\omega}^B \times \left(\boldsymbol{I}\boldsymbol{\omega}^B\right)\right), \tag{31}$$

where $\boldsymbol{I}$ is the inertia tensor and $\boldsymbol{M}$ is the applied moment. Finally, the full kinematics of the reduced attitude can be expressed by substituting Eq. (31) into Eq. (27).

Both the INDI and ANDI control laws (Eq. (13) and Eq. (17), respectively) require an expression for the control effectiveness matrix $\boldsymbol{F}_{u_{n^B}}$ to regulate $(\ddot{\boldsymbol{n}}|_B)^B$. Specifically, differentiating the term $\boldsymbol{H}_B\dot{\boldsymbol{\omega}}^B$ with respect to the control input yields:

$$\boldsymbol{F}_{u_{n^B}} = \frac{\partial\,(\ddot{\boldsymbol{n}}|_B)^B}{\partial \boldsymbol{u}} = \boldsymbol{H}_B\, \frac{\partial \dot{\boldsymbol{\omega}}^B}{\partial \boldsymbol{u}} = \boldsymbol{H}_B\, \boldsymbol{I}^{-1}\, \frac{\partial \boldsymbol{M}(\boldsymbol{u}, \boldsymbol{x})}{\partial \boldsymbol{u}}. \tag{32}$$

To apply ANDI, the state compensation term is also required. This is retrieved via:

$$\boldsymbol{F}_{x_{n^B}} = \frac{\partial\,(\ddot{\boldsymbol{n}}|_B)^B}{\partial \boldsymbol{x}_{\boldsymbol{n^B}}} \tag{33}$$

where

$$\boldsymbol{x}_{\boldsymbol{n^B}} = \left[\boldsymbol{\omega^B}, \boldsymbol{L_{BI}}, \boldsymbol{n}^I, (\dot{\boldsymbol{n}}|_I)^I, (\ddot{\boldsymbol{n}}|_I)^I\right]^T. \tag{34}$$

It then follows that:

$$\begin{aligned}\boldsymbol{F}_{x_{n^B}}\dot{\boldsymbol{x}}_{\boldsymbol{n^B}} = &\,\boldsymbol{\omega}^B \times \left(\dot{\boldsymbol{\omega}}^B \times \boldsymbol{n}^B\right) + 2\dot{\boldsymbol{\omega}}^B \times \left(\boldsymbol{\omega}^B \times \boldsymbol{n}^B\right) \\ &- \boldsymbol{\omega}^B \times \left(\boldsymbol{\omega}^B \times \left(\boldsymbol{\omega}^B \times \boldsymbol{n}^B\right)\right) - 3\dot{\boldsymbol{\omega}}^B \times (\dot{\boldsymbol{n}}|_I)^B \\ &+ 3\boldsymbol{\omega}^B \times \left(\boldsymbol{\omega}^B \times (\dot{\boldsymbol{n}}|_I)^B\right) - 3\boldsymbol{\omega}^B \times (\ddot{\boldsymbol{n}}|_I)^B + (\dddot{\boldsymbol{n}}|_I)^B \\ &- \boldsymbol{I}^{-1}\left[\dot{\boldsymbol{\omega}}^B \times \left(\boldsymbol{I}\boldsymbol{\omega}^B\right) - \boldsymbol{\omega}^B \times \left(\boldsymbol{I}\dot{\boldsymbol{\omega}}^B\right)\right].\end{aligned} \tag{35}$$

http://www.imavs.org/

http://www.imavs.org/

Finally, it is important to note that an INDI or ANDI reduced attitude controller is not strictly limited to fault-case scenarios; it can also be used under nominal conditions. A standard nominal controller allocates for the body z-axis acceleration a_z alongside the angular accelerations $\dot{p}$, $\dot{q}$, and $\dot{r}$. By simply replacing the targets for $\dot{p}$ and $\dot{q}$ with the x and y components of $(\ddot{\boldsymbol{n}}|_B)^B$, the modified controller not only retains full nominal flight capabilities but also inherently supports the stabilization of spinning bodies. However, employing this relaxed attitude structure requires a different Error Controller (EC) than that of a nominal controller, which will be discussed in the next section.

6 CONTROLLER DESIGN

The controller, whether based on INDI or ANDI, adopts a cascaded structure consisting of an inner stabilization loop and an outer guidance loop. The objective of the stabilization controller is to realize a desired linear acceleration vector. To achieve this, its first task is to align the principal axis of rotation $\boldsymbol{\mu}^B$ with the desired inertial unit vector $\boldsymbol{n}^I$, which represents the direction of the desired specific force expressed in the inertial frame. This principal axis arises from the relaxed-hover equilibrium solution and, in the case of two opposing motor failures, is aligned with the body z-axis, i.e., $\boldsymbol{\mu}^B = [0, 0, -1]^T$ [1]. The controller must then ensure that the magnitude of the generated acceleration is also correct by modulating the total thrust. Finally, when the vehicle is not operating under fault conditions, a desired yaw acceleration can also be tracked. Hence, the subset of controlled variables, for which desired inputs are provided in the pseudo-control vector for both control laws, is:

$$\boldsymbol{x} = \left[a_z, (\ddot{n}|_B)^B_x, (\ddot{n}|_B)^B_y, \dot{r}\right]^T. \tag{36}$$

The innermost control loop in which the two control laws are applied to regulate $\boldsymbol{x}$ is shown in Figure 5. The signals shown in red are present only in the ANDI implementation. The control increment $\boldsymbol{\Delta u}$ is computed through a Weighted Least Squares (WLS) allocator [21, 22]. This routine is commonly used to handle actuator saturation while also establishing a hierarchy among control objectives through the pseudo-control weighting matrix $\boldsymbol{W_v}$. By setting specific diagonal entries of $\boldsymbol{W_v}$ to zero, the corresponding control axes are effectively relaxed in the WLS cost function. This makes it possible to discard axes that cannot be controlled under fault conditions. For example, yaw is always sacrificed, while either $(\ddot{n}|_B)^B_x$ or $(\ddot{n}|_B)^B_y$ is relaxed depending on whether the failed motors correspond to the roll or pitch axis.

As for the computation of $\boldsymbol{\nu}$, a linear error controller

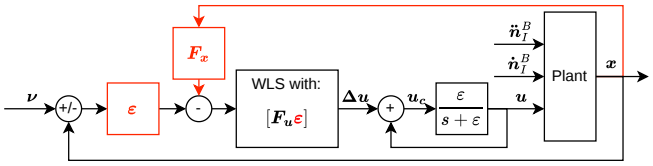


Figure 5: Allocation diagram. Red signals and variables are additional in ANDI compared to INDI.

based on Eq. (23) and Eq. (26) is used, such that:

$$\boldsymbol{\nu} = \begin{bmatrix} a_{z_d} \\ (\ddot{n}|_B)^B_{x_d} \\ (\ddot{n}|_B)^B_{y_d} \\ \dot{r}_d \end{bmatrix} = \begin{bmatrix} a_{z_d} \\ k_1^s k_2^s \left(\mu_x^B - n_x^B\right) - k_2^s \left(\dot{n}|_B\right)^B_x \\ k_1^s k_2^s \left(\mu_y^B - n_y^B\right) - k_2^s \left(\dot{n}|_B\right)^B_y \\ k_1^s k_2^s \left(\psi_d - \psi\right) - k_2^s r \end{bmatrix}. \tag{37}$$

The desired acceleration magnitude a_{z_d}, together with its direction, is computed by the outer-loop guidance controller shown in Fig. 6.

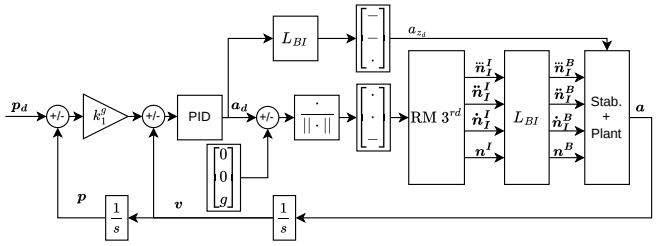


Figure 6: Guidance controller.

The proposed method employs a Reference Model (RM) that maps the desired n^I into smooth, time-synchronized reference trajectories for the desired principal axis and its derivatives. This avoids relative delays between the signals, which is critical for state estimation within the stabilization controller. Moreover, the guidance structure consists of a velocity PID loop nested inside an outer proportional position loop. Finally, Table 2 reports the gains used in the presented control loops.

k_1^s	k_2^s	k_1^g	k_P^g	k_I^g	k_D^g
4.2	10.0	0.6	1.8	0.4	0.2

Table 2: Parameters used in the controllers.

7 FLIGHT TESTS

To evaluate the ANDI and INDI controllers, and to analyze their differences in order to draw meaningful conclusions, flight tests were conducted at the indoor test facility of TU Delft, shown in Fig. 7. Attitude and position are estimated using an external motion-capture system running at approximately 80 Hz. All data files and processing scripts are accessible at [23].



Figure 7: Test platform flying in the Cyberzoo, the indoor test facility of TU Delft.

The failure scenario considered in this work is a complete loss of active control authority of the front and back motors. The left and right motors are then responsible for stabilizing and guiding the platform under fault conditions, while the drone spins about its body z-axis. In contrast, the front and back motors are only passively modulated to produce a faster or slower spin and are not used for stabilization; indeed, they are always commanded identically.

The first test is designed to identify the yaw rate at which each controller loses the ability to stabilize the drone. To this end, the drone is commanded to hold a fixed position in space while the front and back motors are slowly commanded a continuously decreasing setpoint. Figure 8 and Figure 9 show the motor commands and the resulting yaw rate for the INDI and ANDI controllers, respectively.

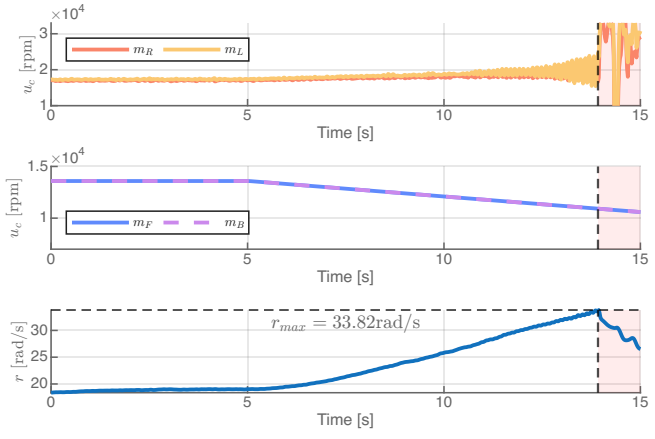


Figure 8: Motor commands and yaw rate in the loss of control test of the INDI controller. The red area indicates that loss of control has occurred.

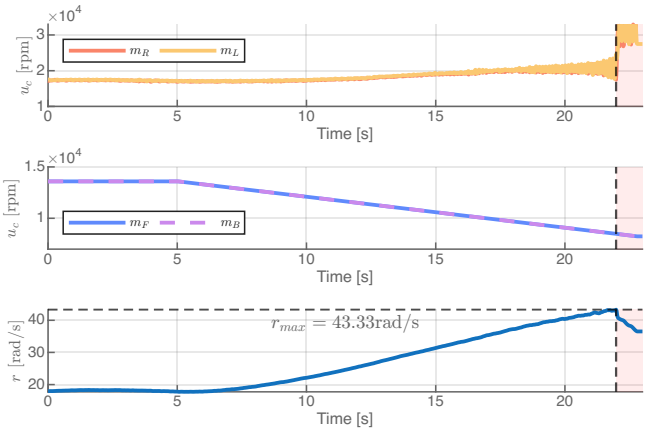


Figure 9: Motor commands and yaw rate in the loss of control test of the ANDI controller. The red area indicates that loss of control has occurred.

For both controllers, the steadily decreasing command to the pitch motors produces a progressively increasing yaw rate. Notably, the INDI controller loses stability at $33.82\,\mathrm{rad\,s^{-1}}$, while the ANDI controller remains stable up to a considerably higher rate of $43.33\,\mathrm{rad\,s^{-1}}$. As the drone spins faster, the gyroscopic coupling induced by the state grows larger, and failing to account for it in the INDI control law leads to a progressive degradation in allocation accuracy. The ANDI controller, by explicitly compensating for this term, is able to maintain stable flight at higher spin rates. Nevertheless, ANDI eventually also experiences a loss of control, which is to be expected. As discussed in Section 4, ANDI does not alter the actuator dynamics; rather, it ensures that the innermost allocation loop follows those dynamics. It is worth noting that the spin rate of $43.33\,\mathrm{rad\,s^{-1}}$ already exceeds the $29\,\mathrm{rad\,s^{-1}}$ corner frequency of the actuator dynamics, at which point the actuator transfer function exhibits an attenuation of $-4.9\,\mathrm{dB}$ and a phase delay of $55.4\,^\circ$. As the spin rate increases further beyond this threshold, the attenuation and phase delay grow, and the ANDI controller will inevitably also fail.

Another conclusion drawn from the test is that both controllers are expected to successfully stabilize the drone at lower spin rates. It is therefore interesting to analyze whether there are noticeable differences between the two controllers in such conditions. To investigate this, the performance of both controllers is compared in a task involving flying a square trajectory at a yaw rate of approximately $20\,\mathrm{rad\,s^{-1}}$, which is achieved by commanding a constant setpoint to the pitch motors. Figure 10 shows the position tracking and the resulting yaw rate for both the INDI and ANDI controllers.

As expected, Fig. 10 demonstrates that both controllers are capable of accurately tracking the square trajectory at a spin rate of roughly $20\,\mathrm{rad\,s^{-1}}$. Furthermore, Fig. 11 and Fig. 12 reveal that this performance is enabled by the accu-

http://www.imavs.org/

http://www.imavs.org/

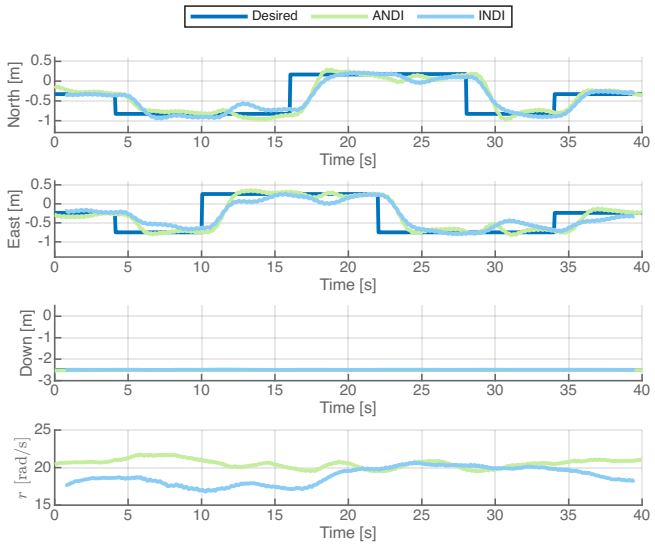


Figure 10: Position tracking comparison of a square trajectory with the INDI and ANDI controllers.

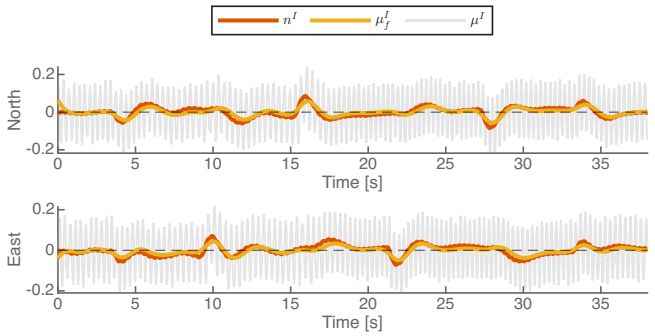


Figure 11: Principal axis of rotation tracking with the INDI controller.

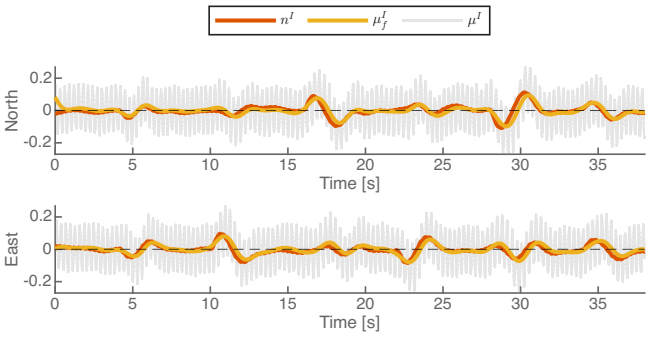


Figure 12: Principal axis of rotation tracking with the ANDI controller.

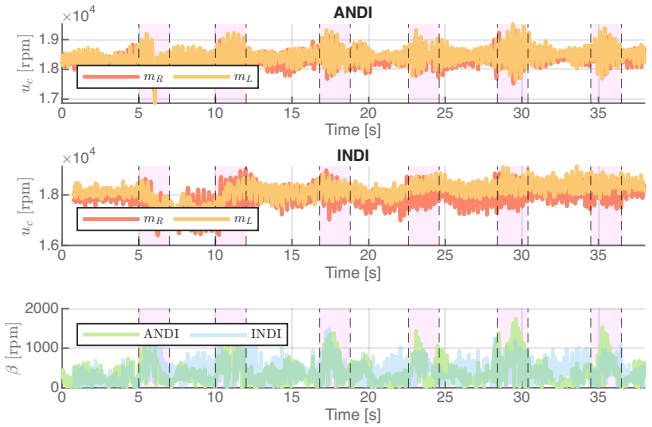


Figure 13: Comparison of control effort during the square tracking task between the INDI and ANDI controllers. Shaded areas indicate time intervals in which the drone is actively moving.

rate tracking of the desired inertial direction $\boldsymbol{n}^I$ using the projection of the principal axis of rotation onto the inertial frame, $\boldsymbol{\mu}^I$. However, while both controllers appear to perform very similarly in this task, there are subtle differences between them, which are elucidated in Fig. 13.

The commanded signals to the left and right motors during the square tracking test for both the INDI and ANDI controllers are presented in Figure 13. It also illustrates the variance of the control effort for the actuated axis, which is calculated as:

$$\hat{u}_c = u_{c_{m_L}} - u_{c_{m_R}}, \quad \beta = \left\| \hat{u}_c - \underline{\hat{u}_c} \right\|, \tag{38}$$

where $\underline{\hat{u}_c}$ denotes the moving average of $\hat{u}_c$. Thus, β serves as a measure of how much the control effort oscillates around its mean.

The results in Figure 13 show that during the intervals when the drone is actively moving and accelerating, the required control effort is generally higher for ANDI than for INDI. This behavior is expected, as the gyroscopic effect naturally opposes changes to the principal axis of rotation. Because ANDI explicitly compensates for this effect in advance, it computes a higher commanded effort to force the required motion.

Interestingly, however, during the intervals when the drone is stationary at the vertices of the square, where the controller is simply regulating its position and rejecting disturbances, the control effort is instead higher for INDI. As established in Section 4, at a yaw rate of $20\,\mathrm{rad\,s^{-1}}$, the control bandwidth of the angular acceleration in INDI is already degraded. This higher control effort indicates poorer control allocation; even when the drone is nominally hovering in place, INDI must continuously compensate for its own allocation inaccuracies, resulting in greater overall actuator activity.

Finally, ANDI was tested on a square trajectory above INDI's maximum stable spin rate of $33.82\,\mathrm{rad\,s^{-1}}$. Figures 14 and 15 confirm that ANDI successfully maintains accurate tracking at the yaw rate of roughly $34.5\mathrm{rad\,s^{-1}}$.

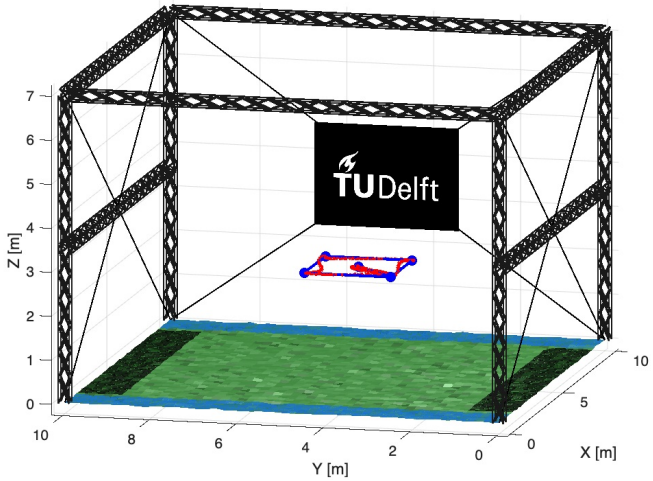


Figure 14: 3D flight path of the square trajectory using the ANDI controller at an average spin rate of $34.5\,\mathrm{rad\,s^{-1}}$ recorded at the Cyberzoo.

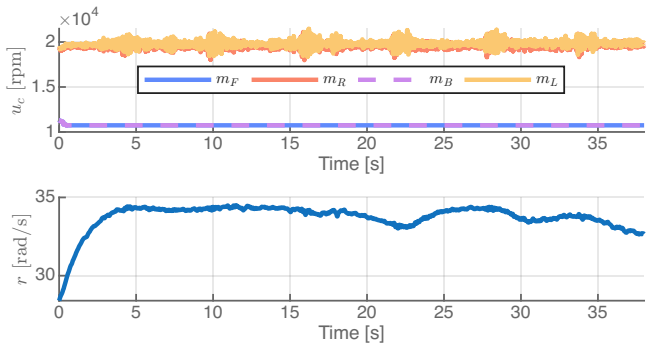


Figure 15: Command signals and yaw rate during the ANDI square tracking test at high spin rate.

8 CONCLUSION

This paper has demonstrated that the proposed ANDI controller can successfully guide and stabilize a quadcopter experiencing a complete loss of control authority in two opposing motors. The proposed framework was theoretically analyzed, verified in simulation, and validated through real-world flight tests, drawing a direct performance comparison with a comparable INDI architecture previously documented in the literature.

The results demonstrate that by explicitly incorporating knowledge of actuator dynamics and the kinematics of a spinning body into the control allocation, the ANDI controller successfully compensates for state-induced gyroscopic effects. Consequently, the ANDI framework is capable of maintaining stable flight and accurate trajectory tracking at significantly higher spin rates than INDI, which suffers from progressive allocation degradation under identical conditions. For platforms characterized by high required spin rates and relatively slow actuators, this extended operational range marks the difference between successfully executing a relaxed-hover solution and experiencing a total loss of control. An additional advantage of the ANDI controller is observed in its efficiency during stationary flight; the ANDI framework exhibits a lower overall control effort variance compared to INDI, indicating superior control allocation accuracy and a reduction in unnecessary actuator compensation.

Future work should focus on a rigorous robustness analysis to determine the extent to which the ANDI controller retains its performance advantages under severe model inaccuracies, parametric uncertainties, and unmodeled delays.

ACKNOWLEDGEMENTS

This research was co-funded by the Royal Dutch Navy and the Dutch Coast Guard. This initiative aims to foster collaboration and innovation in maritime endeavors.

REFERENCES

[1] Mark W. Mueller and Raffaello D'Andrea. Stability and control of a quadrocopter despite the complete loss of one, two, or three propellers. In *2014International Conference on Robotics and Automation (ICRA)*, pages 45–52, Hong Kong, China, May 2014. IEEE.

[2] Mark W. Mueller and Raffaello D'Andrea. Relaxed hover solutions for multicopters: Application to algorithmic redundancy and novel vehicles. *The International Journal of Robotics Research*, 35(8):873–889, 2016.

[3] Sihao Sun, Leon Sijbers, Xuerui Wang, and Coen de Visser. High-Speed Flight of Quadrotor Despite Loss of Single Rotor. *IEEE Robotics and Automation Letters*, 3(4):3201–3207, October 2018.

[4] Sihao Sun, Xuerui Wang, Qiping Chu, and Coen de Visser. Incremental Nonlinear Fault-Tolerant Control of a Quadrotor With Complete Loss of Two Opposing Rotors. *IEEE Transactions on Robotics*, 37(1):116–130, February 2021.

[5] E. J. J. Smeur, G. C. H. E. de Croon, and Q. Chu. Cascaded incremental nonlinear dynamic inversion for MAV disturbance rejection. *Control Engineering Practice*, 73:79–90, April 2018.

[6] Ole Pfeifle and Walter Fichter. Cascaded Incremental Nonlinear Dynamic Inversion for Three-Dimensional Spline-Tracking with Wind Compensation. *Journal of Guidance, Control, and Dynamics*, 44(8):1559–1571, August 2021.

[7] Tomaso M. L. De Ponti, Ewoud J. J. Smeur, and B. W. D. Remes. Incremental Nonlinear Dynamic Inversion controller for a Variable Skew Quad Plane. In

http://www.imavs.org/

2023 International Conference on Unmanned Aircraft Systems (ICUAS), pages 241–248, June 2023.

[8] P. Simplício, M. D. Pavel, E. van Kampen, and Q. P. Chu. An acceleration measurements-based approach for helicopter nonlinear flight control using Incremental Nonlinear Dynamic Inversion. *Control Engineering Practice*, 21(8):1065–1077, August 2013.

[9] Ewoud J.J. Smeur, Guido C.H.E. De Croon, and Qiping Chu. Gust disturbance alleviation with Incremental Nonlinear Dynamic Inversion. In *IEEE/RSJ International Conference on Intelligent Robots and Systems*, pages 5626–5631, October 2016.

[10] Ewoud J. J. Smeur, Qiping Chu, and Guido C. H. E. de Croon. Adaptive Incremental Nonlinear Dynamic Inversion for Attitude Control of Micro Air Vehicles. *Journal of Guidance, Control, and Dynamics*, 39(3):450–461, March 2016.

[11] Tomaso M. L. De Ponti, Ewoud J. J. Smeur, and B. W. D. Remes. Incremental nonlinear fault-tolerant control of the variable skew quad plane with loss of two opposing rotors. In *2026 International Conference on Unmanned Aircraft Systems (ICUAS)*, pages 241–248, June 2026.

[12] S. Sieberling, Q. P. Chu, and J. A. Mulder. Robust Flight Control Using Incremental Nonlinear Dynamic Inversion and Angular Acceleration Prediction. *Journal of Guidance, Control, and Dynamics*, 33(6):1732–1742, November 2010.

[13] Stefan A. Raab, Jiannan Zhang, Pranav Bhardwaj, and Florian Holzapfel. Consideration of Control Effector Dynamics and Saturations in an Extended INDI Approach. In *AIAA Aviation 2019 Forum*. June 2019.

[14] Agnes Steinert, Stefan Raab, Simon Hafner, Florian Holzapfel, and Haichao Hong. From fundamentals to applications of incremental nonlinear dynamic inversion: A survey on INDI – Part I. *Chinese Journal of Aeronautics*, April 2025.

[15] Pranav Bhardwaj, Stefan A. Raab, and Florian Holzapfel. Higher Order Reference Model for Continuous Dynamic Inversion Control. In *AIAA Scitech 2021 Forum*, January 2021.

[16] Rasmus Steffensen, Agnes Steinert, and Ewoud J. J. Smeur. Nonlinear Dynamic Inversion with Actuator Dynamics: An Incremental Control Perspective. *Journal of Guidance, Control, and Dynamics*, 46(4):709–717, 2023.

[17] Yue Liu, Agnes Steinert, Haichao Hong, Hangxu Li, and Shiqiang Hu. Nonlinear dynamic inversion with generalized actuator dynamics: Performance and stability. *Aerospace Science and Technology*, 162:110218, July 2025.

[18] Tomaso Maria Luigi De Ponti, Ewoud Jan Jacob Smeur, and Bart Diane Walter Remes. Unified-actuator nonlinear dynamic inversion controller for the variable skew quad plane. *Journal of Guidance, Control, and Dynamics*, 48(5):1167–1176, 2025.

[19] Tomaso De Ponti, Simon Hafner, Ewoud Smeur, and Bart Remes. Actuator nonlinear dynamic inversion for the variable skew quad plane with heterogeneous motor dynamics. *Control Engineering Practice*, 171:106858, 2026.

[20] Justin P. G. Dubois, Evangelos Ntouros, and Ewoud J. J. Smeur. Full actuator nonlinear dynamic inversion for enhanced hybrid uav control. In *2026 International Conference on Unmanned Aircraft Systems (ICUAS)*, pages 241–248, June 2026.

[21] Ola Härkegård. Efficient active set algorithms for solving constrained least squares problems in aircraft control allocation. In *Proceedings of the 41st IEEE Conference on Decision and Control, 2002*, pages 1295–1300. IEEE, 2002.

[22] Ewoud Smeur, Daan Höppener, and Christophe De Wagter. Prioritized control allocation for quadrotors subject to saturation. In *International Micro Air Vehicle Conference and Flight Competition 2017*, pages 37–43, 2017.

[23] Tomaso De Ponti. Test data of actuator nonlinear fault-tolerant control of a fast-spinning quadrotor with loss of two opposing rotors, 2026.

http://www.imavs.org/